Long-term evaluation of solid oxide fuel cell candidate materials in a 3-cell generic stack test fixture, part III: Stability and microstructure of Ce-(Mn,Co)-spinel coating, AISI441 interconnect, alumina coating, cathode and anode

Yeong-Shyung Chou*, Jeffry W. Stevenson, Jung-Pyung Choi

K2-44, Energy and Efficiency Division, Pacific Northwest National Laboratory, P. O. Box 999, Richland, WA 99354, USA

HIGHLIGHTS

- Ce-(Mn,Co) spinel coating on AISI441 metal was examined after 800 °C 6000 h^{-1}.
- Alumina coating strongly bonded to the metal substrate without spallation.
- EDS analysis showed no Cr depletion in AISI441.
- Mutual diffusion observed between welded Ni wire and AISI441 interconnect.
- Small Cr was only detected at cathode and was discussed with performance.

ABSTRACT

A generic solid oxide fuel cell stack test fixture was developed to evaluate candidate materials and processing under realistic conditions. Part III of the work investigated the stability of Ce-(Mn,Co) spinel coating, AISI441 metallic interconnect, alumina coating, and cell's degradation. After 6000 h test, the spinel coating showed densification with some diffusion of Cr. At the metal interface, segregation of Si and Ti was observed, however, no continuous layer formed. The alumina coating for perimeter sealing areas appeared more dense and thick at the air side than the fuel side. Both the spinel and alumina coatings remained bonded. EDS analysis of Cr within the metal showed small decrease in concentration near the coating interface and would expect to cause no issue of Cr depletion. Inter-diffusion of Ni, Fe, and Cr between spot-welded Ni wire and AISI441 interconnect was observed and Cr-oxide scale formed along the circumference of the weld. The microstructure of the anode and cathode was discussed relating to degradation of the top and middle cells. Overall, the Ce-(Mn,Co) spinel coating, alumina coating, and AISI441 steel showed the desired long-term stability and the developed generic stack fixture proved to be a useful tool to validate candidate materials for SOFC.

© 2013 Published by Elsevier B.V.

1. Introduction

Recent advances in anode-supported thin electrolyte cells have greatly reduced the operating temperatures from ~1000 °C to ~800 °C for planar solid oxide fuel cells (SOFCs) [1–3]. At these temperatures the use of low-cost and durable metallic interconnect materials becomes possible as compared to brittle ceramic materials such as LaCrO$_3$, which is fragile and difficult to form and sinter. To minimize the residual stresses from the coefficient of thermal expansion (CTE) mismatch with the anode-supported cells, ferritic stainless steel with appreciable amount of Cr has been widely studied as a leading candidate alloy due its oxidation resistance and ability to form a conductive scale in oxidizing environment. Ferritic steels such as Crofer22APU, AISI441, SS430, Ebrite and others have been studied [4–13]. Although Cr$_2$O$_3$ is conductive at SOFC operating temperatures, the electrical conductivity is much lower than the base metal and Ni at the anode side [14], as well as typical cathode and contact materials. Also, the well known Cr-poisoning effect on cathodes forbids the direct use of these metals without a protective conducting coating [15–19]. A novel (Mn,Co)$_3$O$_4$ spinel was therefore developed for ferritic stainless steels that shows high conductivity, matching CTE and long-term stability with both

* Corresponding author. Tel.: +1 509 3752527; fax: +1 509 3752186.
  E-mail address: yeong-shyung.chou@pnnl.gov (Y.-S. Chou).

Crofer22APU and AISI441 substrates [20–26]. However, even with the protective $(Mn,Co)_3O_4$ spinel coating, Cr-containing oxide scales still form on these ferritic stainless steel substrates over time, and can spall off upon repeated thermal cycling. To mitigate the adhesion issue, a small amount of rare earth of Ce was added to the $(Mn,Co)_3O_4$ spinel and small coupon tests showed similar conductivity and stability [25]. In addition to the conductive coating to protect the cell's electrochemical performance, an insulating protective coating was also required for the sealing area in which no electrical current was allowed to pass. This insulating coating was intended to block the chemical reaction of Cr with alkaline earths such as Ba and Sr in sealing glasses to form undesirable chromate phases of very high CTE [27–29]. These chromates are thermodynamically favored to form in oxidizing environments and can lead to seal failure which then can cause the cell or stack failure. These candidate materials, Ce-$(Mn,Co)_3O_4$ spinel coating, aluminization, and AISI441 interconnect, have been mostly studied in small button-sized cells, not in a realistic SOFC stack environment. It is therefore the objective of this work to study these candidate materials in a generic stack fixture to fully assess their stabilities and interactions with mating materials for long-term operation. Part one of the work reported the design of a generic stack fixture, cell assembly, seal system, and each cell's performance [30]. Part two of the work studied the sealing glass stability and chemical compatibility with YSZ and aluminized AISI441 interconnect [31]. Part three of the work will address the integrity of Ce-$(Mn,Co)_3O_4$ spinel coating, aluminization, AISI441 interconnect, as well as cathode and anode microstructure changes relating to cell degradation.

2. Experimental

2.1. Materials, processing and short-stack assembly

A 3-cell short stack was assembled for the long-term stability test at 800 °C using the generic stack test fixture. A commercial anode supported thin YSZ electrolyte cell of 50 mm × 50 mm × 0.5 mm with LSM−YSZ composite cathode was used. The cells were sealed onto aluminized AISI441 window frames with refractory sealing glass YSO77 and stacked together with hybrid micas as perimeter seal. LSM and NiO were used as cathode and anode contact, respectively. Ni mesh was also used as the anode current collector while no metallic mesh was used at the cathode side. Ferritic stainless steel AISI441 was used for the interconnect plates and window frames. Aluminization was applied to the AISI441 on areas requiring no electrical conduction, and Ce-(Mn,Co) spinel coating was applied in the central section facing the cathode. The details of the cell, materials, coatings, processing and stack firing are given in Ref. [30].

2.2. Post-mortem characterization

After the 800 °C 6000 h test, the short stack was dis-assembled and post-mortem analysis was conducted with optical microscopy and scanning electron microscopy with energy dispersion spectroscopy (JOEL SEM model 5900LV). Characterization with optical microscopy was reported in part I with respect to seal failure, cathode and anode morphology, and contact materials [30]. In part II the materials' characterization was focused on refractory sealing glass microstructure stability and interfacial reactions at YSZ and aluminized AISI441 interfaces. In this work, the microstructure at the Ce-(Mn,Co)-spinel coated interface and its effect in blocking Cr diffusion was studied at the contact site with LSM (spot #1 in Fig. 1). To validate the aluminization coating and Cr depletion issue, the uncovered (by LSM contact) areas were also examined both in the air and fuel side as shown at #2 and #3, respectively, in Fig. 1. In addition, the Ni mesh spot-welded onto AISI441 plate as current
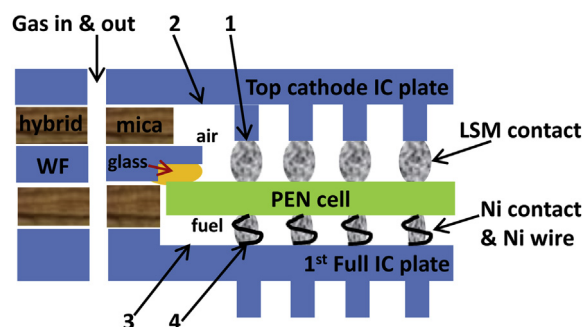

Fig. 1. Schematic drawing showing the top cell assembly with mating AISI441 interconnect plates. Four locations (#1−#4) were selected for microstructure characterization. The locations corresponding to anode and cathode microstructure characterization are not shown.

collector was investigated as #4. These locations are related to the top cell and corresponding interconnect plates as shown in Fig. 2 of Ref. [30]. In addition to the coatings and AISI441 interconnect metal, the microstructure of cathode and anode from the top cell and middle cell was also investigated with electron scanning microscopy. The preparation of metallurgical samples was given in
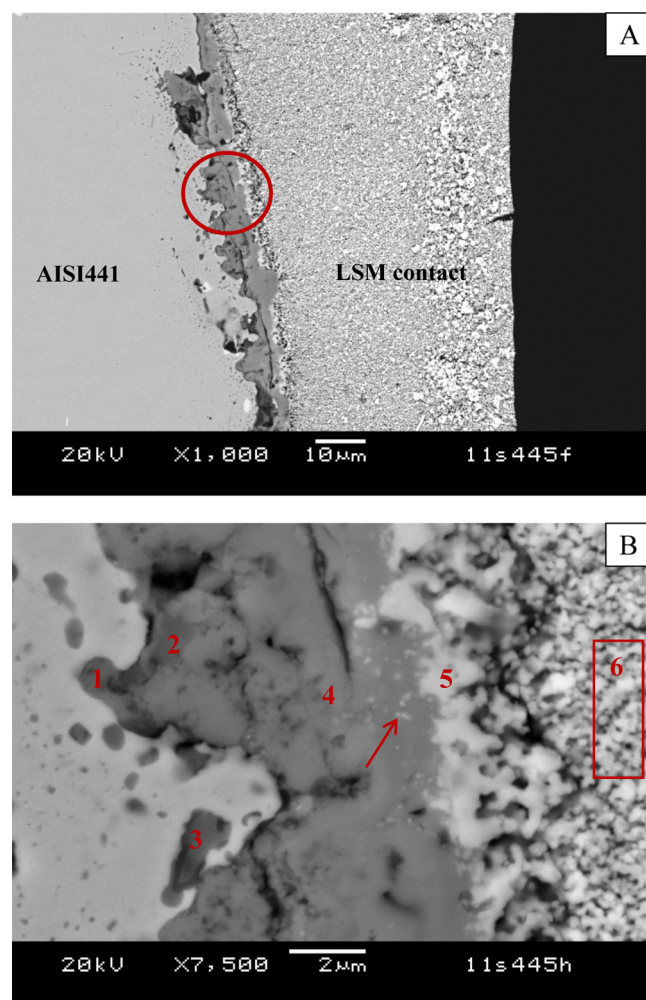
Fig. 2. Microstructure of Ce-(Mn,Co)-spinel coating between AISI441 interconnect and LSM contact after 800 °C 6000 h^{-1} cell test, (A) low magnification and (B) high magnification of the circled area in (A). The arrow in (B) shows the CeO_2 sub-micron particles. EDS spot and area analyses are listed in Table 1.
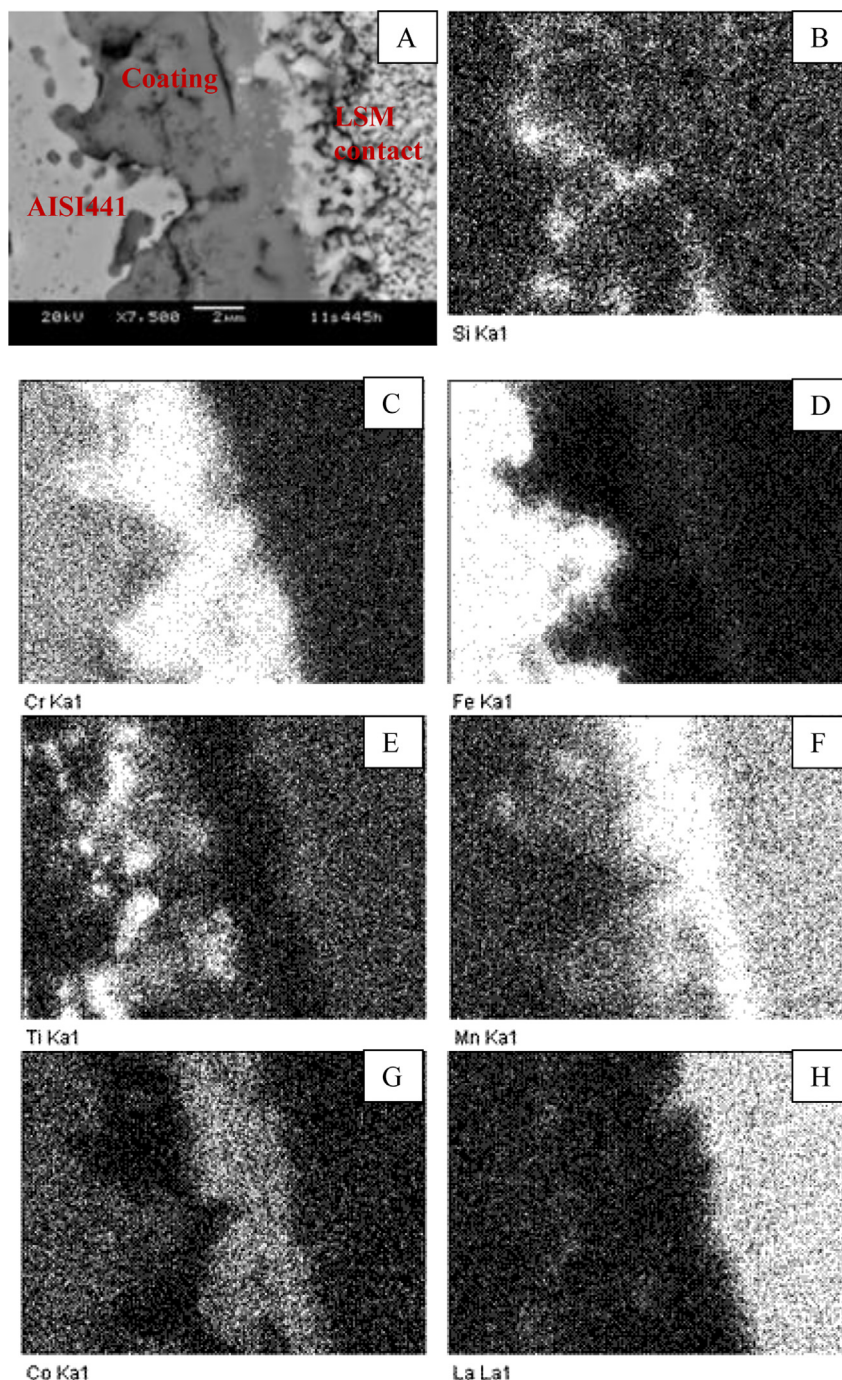
Fig. 3. Elemental mapping of Ce-(Mn,Co) spinel coating, (A) corresponding SEM micrograph, (B) Si, (C) Cr, (D) Fe, (E) Ti, (F) Mn, (G) Co, and (H) La.

detail in Ref. [31]. During the test, cell impedance was also characterized about every 500 h using an impedance analyzer (Model VSP and VMP3B, Bio-Logic SA, Princeton Applied Research, Oak Ridge, TN) and frequencies between 20 kHz and 40 MHz at constant voltage of 0.8 V.

3. Results and discussion

3.1. Ce-(Mn,Co)-spinel coating

A Ce-modified (Mn,Co)-spinel coating was applied to AISI441 interconnect plates to provide electrical conduction while blocking

Cr diffusion. The addition of a small amount of Ce was to improve the adhesion of the Cr-oxide scale that grew underneath the coating during the test. The microstructure of the coating in contact with LSM cathode contact (location #1 in Fig. 1) is shown in Fig. 2 and the elemental mappings of species of interest are shown in Fig. 3. At low magnification of the interfacial microstructure, no debonding was observed between the spinel coating and LSM contact. This is likely due to the initial porous microstructure of the spinel coating with rough surface texture from the ultrasonic spraying process, which offered mechanical interlocking and inter-diffusion between the spinel and LSM. The (Mn,Co)-spinel coating also appeared strongly bonded to the AISI441 substrate and was

Table 1
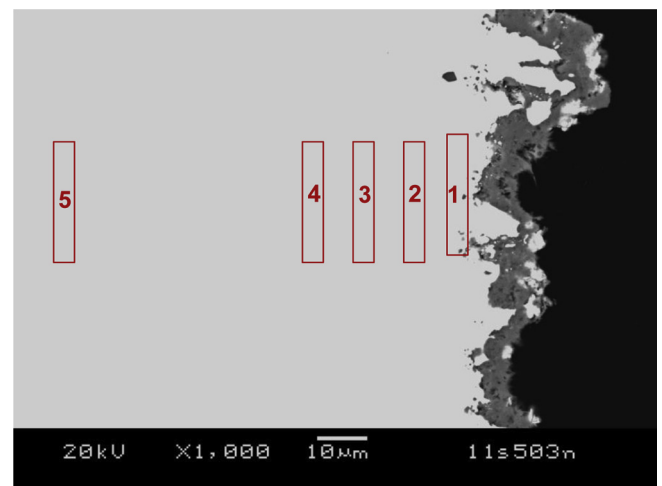Chemical analyses of spots and areas #1–#6 in Fig. 2B.

Spot#	O	Mg	Si	Ca	Ti	V	Cr	Mn	Fe	Co	Sr	La
1	56.50	0.81	2.14	0.33	5.39		19.79	4.33	10.71			
2	68.66		1.08	0.18	11.47		16.40	0.85	1.35			
3	49.04		2.26		17.77	0.94	8.49		21.50			
4	63.55		1.46		1.04		26.02	3.94	0.42	3.56		
5	62.01				1.38		0.61	16.46	0.82	1.26	3.11	14.35
6	60.45							18.25		0.89	3.53	16.88

denser than the initial microstructure with ∼20−30% porosity [22,32]. Rare earths (RE) such as La and Ce have been demonstrated to improve the Cr-oxide scale adhesion either through the alloying process or by deposition of RE as an oxide directly onto the metal substrate [33,34]. The current one coating process (i.e., Ce and spinel combined) appeared more advantageous and seemed to be effective to keep the underneath Cr-oxide scale from spalling off. The small amount of sub-micron CeO_2 (∼2−5%) particles remained dispersed without coarsening as shown by the arrow in Fig. 2B, indicating its stability within the host (Mn,Co)-spinel matrix. In addition, the relatively small amount and size of the particles did not act as rigid inclusions resisting the densification of (Mn,Co)-spinel. To further examine the effectiveness of the spinel coating in blocking outward diffusion of Cr or other metal species, elemental analyses were conducted, as shown in Fig. 2B. The results are listed in Table 1. The color contrast of the oxide scale at the metal interface appeared very diffuse showing not only Cr but also other species as Ti and Si (spots #1−#3). The diffusion of Cr seemed limited in that the Cr concentration decreased substantially to 0.61 at% at about 6 microns from the interface (spot #5), and no Cr was detected in the LSM contact area (#6). The elemental mapping also confirmed the outward diffusion of Si, Ti, and Cr was limited to the interfacial region and the spinel coating (Fig. 3B, C, and E, respectively). Examination of Fig. 3C, F, and G indicates the presence of a Cr-based oxide scale that also included an appreciable amount of Mn, which is consistent with previously published results for AISI441 and other ferritic stainless steels. Ti and Si appeared to be localized at the interface between AISI441 and Cr-oxide scale, which is also consistent with previous results. Similar interfacial microstructure was observed by Jablonski et al. who studied the effect of Nb on the formation of Laves phase on AISI441. For the standard AISI441 which contained 0.5 wt% Nb, isolated Si-rich and Ti-rich phases were found after exposing in air for 1000 h at 800 °C. For AISI441 without Nb, the Si tended to form a thin and resistive continuous subscale [6]. No distinct Fe and La diffusion was observed (Fig. 3D and H). The concentration of Co seemed uniform within the (Mn,Co)-spinel coating (Fig. 3G), although Mn showed a higher concentration near the LSM contact (Fig. 3F). The microstructure characterization clearly showed the desired densification of the spinel coating and the prevention of Cr diffusion into the LSM contact. The optimum electrical conductivity of (Mn,Co)-spinel was determined to occur at equal ratios of Mn to Co ($Mn_{1.5}Co_{1.5}O_4$). The 800 °C conductivity was measured to be ∼60 S cm^{-1}; spinel with a small amount of CeO_2 showed similar area specific resistance over 1000 h at 800 °C [24,25]. The conductivity of $MnCr_2O_4$ was ∼2 orders of magnitudes lower than (Mn, Cr)-spinel [23], and ∼3−4
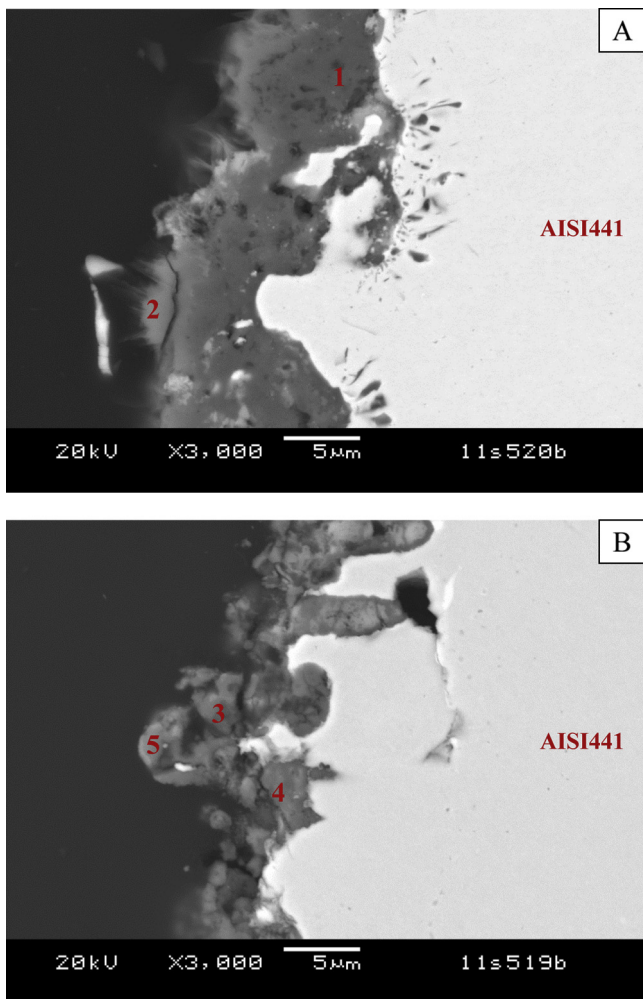
Fig. 4. Typical coating microstructure of aluminized AISI441 after 800 °C 6000 h^{-1} cell test, (A) at air side, and (B) at fuel side corresponding to spots #2 and #3 in Fig. 1, respectively. EDS spot analyses are listed in Table 2.

Fig. 5. Microstructure of aluminized AISI441 interconnect plate not covered by sealing glass. EDS of selected areas (#1–#5) is listed in Table 3.

Table 2
Chemical analyses of spots and areas #1–#5 in Fig. 4 of aluminized AISI441 interconnect not covered by sealing glass.

Spot#	O	Al	Ti	Si	Cr	Fe	K	Ca	Mn	Ba	Sr
1	61.99	37.57	0.07		0.11	0.26					
2	64.66	32.48				0.19	0.81	0.34	0.96	0.41	0.14
3	66.03	28.43		0.27	2.96	2.31					
4	64.09	30.86	0.09		1.52	3.44					
5	64.58	31.05		1.84	0.78	1.26				0.49	

orders of magnitudes lower for Cr_2O_3 [14,35]. Clearly the presence of Cr-oxide scale can greatly reduce the cell's electrochemical performance, and is likely to contribute to the small degradation observed for the top cell, as reported in part one of the work [30].

3.2. Alumina coating for AISI441

In addition to the conducting and protective (Mn,Co)-spinel coating, ferritic stainless steel AISI441 also requires a protective and insulating (or less conducting) coating on areas for sealing, such as cell to window frame glass seal and compressive mica seal in perimeter sections [30]. The integrity and chemical interaction of the alumina coating with refractory sealing glass were reported in part two of the work [31]. As one can see from the simplified drawing of the cell assembly in a stack, there are areas (as shown in spots #2 and #3 in Fig. 1) that are directly exposed to SOFC environments without any coverage by sealing materials. Fig. 4 shows the typical coating microstructure at the air side and fuel side in Fig. 4A and B, respectively. On both sides, the alumina coating appeared strongly bonded to the AISI441 substrate, as no coating spallation was observed. One would expect very large residual stresses to develop between these two dissimilar materials upon cooling, which could cause spallation, given the large mismatch of CTE and elastic modulus between these two materials (CTE of Al_2O_3 is about $8–9 \times 10^{-6}\,°C^{-1}$ while it is $12–13 \times 10^{-6}\,°C^{-1}$ for AISI441, and Young's modulus of Al_2O_3 is about 350–400 GPa and $\sim$200 GPa for the metal). The adhesion of the coating is likely enhanced by the tortuous texture where the coating showed anchor-like "fingers" into the metal substrate (Fig. 4B), which resulted in mechanical interlocking and compressive stresses on the anchors. The coating on the air side appeared slightly thicker than the fuel side and seemed more continuous and homogeneous, while the fuel side coating showed discrete particle-like morphology, similar to the as-aluminized microstructure [22]. The apparent growth at the air side was likely due to the continuation of the aluminization process where the initially diffused Al metal within the metal substrate started to move outward due to high affinity to oxygen. This process was greatly reduced in the fuel environment where the PO_2 was very small. EDS spot analysis (#1–#5 in Fig. 4) showed the coating was primarily Al-oxide with a small amount (a few percent) of Cr and Fe, indicating the effectiveness of alumina coating in blocking Cr outward diffusion, as compared to the (Mn,Co)-spinel coating.

3.3. AISI441 ferritic stainless steel

Ferritic stainless steel AISI441 has a nominal Cr concentration of $\sim$18–20 wt% and trace amounts of Ti, Nb, Si and Mn [26]. The incorporation of Cr into Fe improves the oxidation resistance at elevated temperatures by forming a protective, dense and continuous Cr-oxide scale. Without the protective Cr-oxide scale, Fe will oxidize severely without forming a passive dense Fe-oxide protection layer, which would lead to structural failure. For planar SOFC applications, thinner AISI441 sheets offer lower material cost, easy processing, and low thermal mass for rapid startup, but Cr

depletion may become an issue causing the oxide scale underneath the protective coating to during routine thermal cycling in long-term operations. It is known that the (Mn,Co)-spinel coating can reduce the oxide scale growth but cannot completely stop the oxidation processes. Liu et al. studied the life prediction of coated and uncoated Crofer22AU (a similar material as AISI441) for SOFC applications. Using a Rockwell indenter, they determined the shear strength of coated and uncoated samples. With known scale growth rates, the life predicted for coated Crofer22APU was 15,500 h at 800 °C and 4,747 h for uncoated one [12]. Clearly the predicted life was less than the desired 40,000 h. Fig. 5 shows the typical microstructure of aluminized AISI441 not covered by sealing materials, showing the dense and continuous alumina layer of dark color. Selected areas from the metal/coating interface were analyzed; the chemical compositions are listed in Table 3. Clearly, only regions close to the interface ($\sim$5 μm, #1 in Fig. 5) showed some loss of Cr in that the concentration was 15.98 at%, as compared to the other areas (#2–#5) which showed a fairly constant concentration of $\sim$20 at%. The Cr concentration was also investigated on areas coated with (Mn,Co)-spinel. Similar results to those recorded in Table 3 were obtained and are therefore not listed here. One can therefore conclude the depletion of Cr would not be an issue for coated AISI441 even in thinner sheets.

3.4. Ni mesh as current collector

At the anode side, Ni mesh is widely used as the current collector, especially for planar SOFCs with Ni/YSZ anode-supported thin electrolyte cells. Use of Ni-based current collector offers good conduction and metallurgical bonding with the anode after reduction, and presents no contamination issues. In our long-term test, the Ni mesh was first spot-welded onto the central section of AISI441 interconnect plates where no aluminization was applied. A NiO paste was also applied between the Ni mesh and the cell during stack assembly. Fig. 6 shows the typical microstructure of a spot-welded Ni wire on AISI441 interconnect plate. The Ni wires showed very large grains after 800 °C 6000 h^{-1}, with some grains as large as $\sim$150 μm. The wire also exhibited circumferential pores close to the circumference (arrow in Fig. 6B). These pores were likely due to the redox process that occurred when the Ni wire was partially oxidized during the initial firing of the short-stack assembly. At the Ni/AISI441 welded interface, a gray layer of $\sim$5–10 μm thick containing Cr and Mn oxide scale was found as confirmed by EDS spot analysis (spots #1 and #2 in Fig. 6C and Table 2). The oxide scale (arrow in Fig. 6A) appeared not continuous

Table 3
Selected area chemical analyses in Fig. 5.

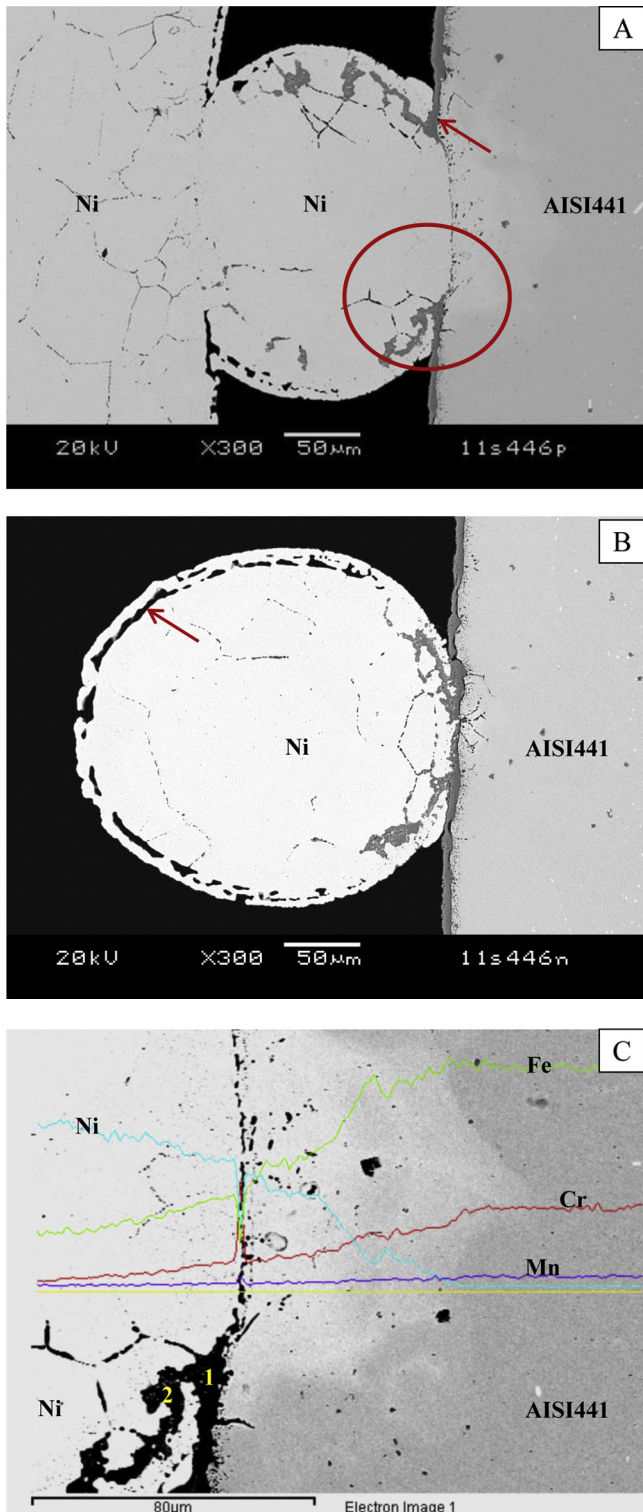| Area#	O	Al	Ti	Si	Cr	Fe
1	10.65	7.44		0.89	15.98	65.03
2				0.88	19.79	79.33
3				0.98	20.18	78.85
4			0.41	0.94	19.81	78.84
5				1.08	19.71	79.21

for Ni wires where the welded section was large (e.g., the welded width was about ∼200 μm). For wires of narrow welding width (∼100 μm in Fig. 6B), the oxide scale seemed continuous. The formation of a continuous oxide scale is likely to degrade the cell's
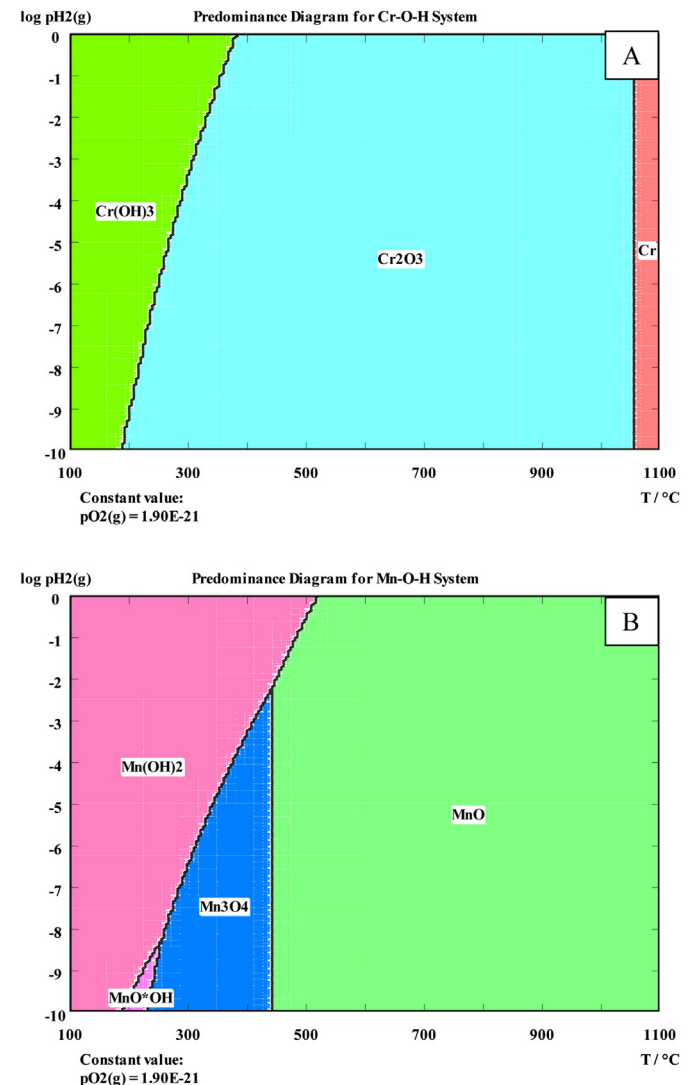

Fig. 6. (A) Microstructure of current collector Ni wire and AISI441 interconnect at spot welded section after 800 °C 6000 h^{-1} test (arrow in (A) shows the Cr-oxide scale). (B) Another welded Ni wire on AISI441 where a dense and continuous Cr-oxide scale formed at the interface. (C) EDS line scans across the circled interfacial area in (A). Spot analyses of #1 and #2 are listed in Table 4.

performance since the oxide scale has much lower conductivity than Ni. For example, the conductivity of thermally grown Cr_2O_3 is about ∼10^{-3}–10^{-4} S cm^{-1} at 800 °C [35]. The oxide scale in Fig. 6 contained both Cr and Mn. The conductivity of Cr–Mn-oxide is not known but would be considered much lower than that of pure Ni (∼300 S cm^{-1}). The oxide scale formed even in the reducing environment where the calculated equilibrium PO_2 was rather low (1.92×10^{-21} atm) for fuel of $H_2:N_2 = 1:1$ with ∼3% H_2O. The observed oxide scale was consistent with thermodynamic calculations (HSC Chemistry software V 5.1 by Outokumpu Research Oy, Finland) of predominant phases for Cr–O–H and Mn–O–H systems in the fuel gas environment, as shown in Fig. 7A and B, respectively. Across the interface, mutual diffusion was evident as shown in Fig. 6C with similar diffusion distance of ∼45 μm for Cr and Ni, while Fe diffused even farther.

### 3.5. Microstructure characterization of cathode and anode

Microstructures of the cathode and anode were also examined after the long-term test. Fig. 8 shows the microstructure of the cathode area from the top cell of the 3-cell short stack, which

Fig. 7. Calculated predominance phase diagram for (A) Cr–O–H and (B) Mn–O–H system at fixed $PO_2 = 1.9 \times 10^{-21}$ atm for fuel of $H_2:N_2 = 1:1$ with 3% H_2O.
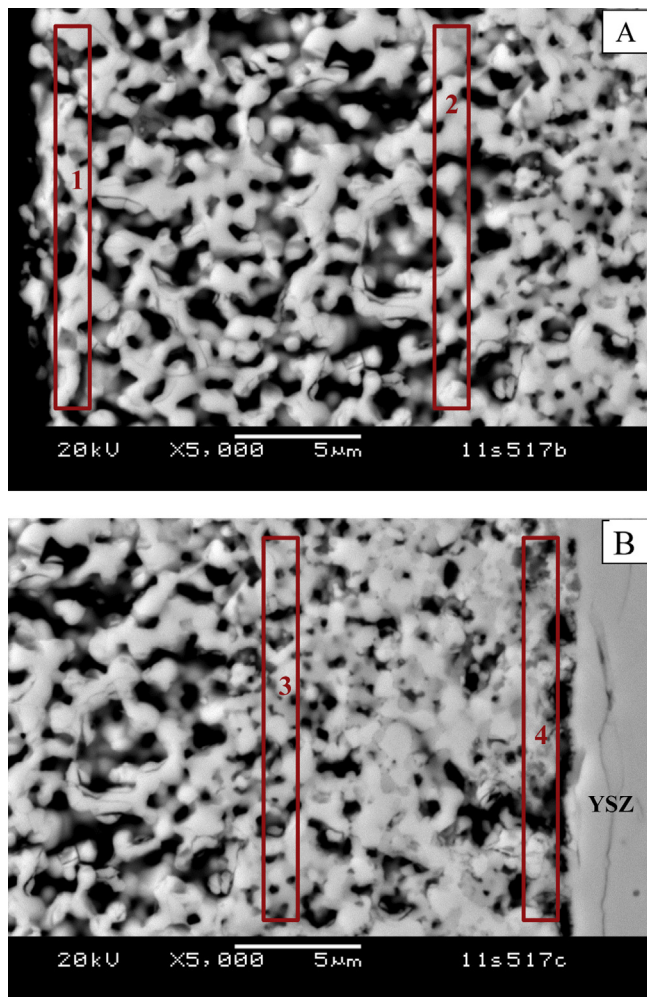
Fig. 8. Cathode microstructure of the top cell (with relatively stable electrochemical performance, see Ref. [30]) of the 3-cell short stack after 800 °C 6000 h^{-1} test, (A) LSM contact layer (between areas #1 and #2), and (B) active layer of LSM–YSZ composite near YSZ electrolyte (between areas #3 and #4). Chemical compositions of selected areas (#1–#4) are listed in Table 5.

showed the most stable electrochemical performance with 1–2% kh^{-1} degradation over 6000 h [30]. Fig. 8A is the LSM cathode current collector (between areas #1 and #2), and Fig. 8B shows the inner active cathode of LSM/YSZ composite next to the YSZ electrolyte (between areas #3 and #4). Selected areas were also subjected to chemical analysis; the results are listed in Table 5. Clearly, no Cr species were identified within the cathode layer. Similar results were also obtained in a few other cathode locations on the 4 cm × 4 cm cathode in that no Cr was detected in areas #1–#3, and no Cr or very small concentration of 0.35 at% (about the detection limit) was found at area #4, i.e., next to YSZ electrolyte. For comparison, the microstructure of the cathode area of the as-received cell before long-term test and the middle cell, which showed much higher degradation than the top cell, is shown in

Table 4
Chemical analyses of spots #1 and #2 in Fig. 6A at the spot-welded Ni wire and AISI441 interconnect interface.

Spot#	O	Si	Cr	Mn	Ni	Nb
1	64.66	0.24	23.02	11.18	0.64	0.26
2	63.32	0.21	22.55	11.06	0.29	2.26

Table 5
Chemical analyses of cathode areas #1–#4 in Fig. 8 after 800 °C 6000 h^{-1} (the sample was from top cell of the short stack which showed the stable performance (Ref. [30])).
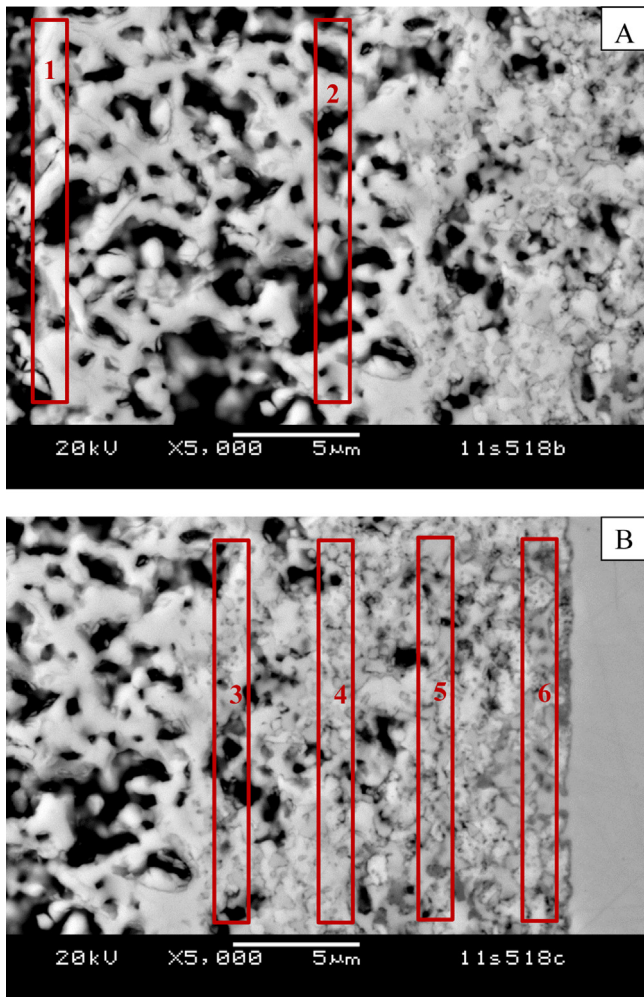
Area#	O	Cr	Mn	Sr	La	Y	Zr	Ni
1	63.80		19.39	3.56	13.25			
2	61.80		18.82	4.13	15.26			
3	66.57		9.15	1.86	7.20	2.65	12.56	
4	67.47		8.31	0.84	5.53	2.93	14.49	0.43

Figs. 9 and 10, respectively. The corresponding chemical analyses within the LSM contact layer and LSM/YSZ composite active layer are listed in Tables 6 and 7, respectively. Examination of the microstructure of the LSM contact layer of the three cells (Figs. 8A, 9A, and 10A) showed no distinct changes in grain sizes and pore sizes, indicating the desired thermal stability of LSM cathode material. This is consistent with the fact that typical sintering temperature for LSM material is greater than 1100 °C, so minimal grain growth would be expected at 800 °C, and Siemens demonstrated tubular cells with LSM cathode with more than 70,000 h operation without significant degradation [36]. EDS analyses also indicated fairly constant La/Sr and (La + Sr)/Mn rations, and no foreign species, especially Cr (Tables 5–7). At the inner active cathode layer of
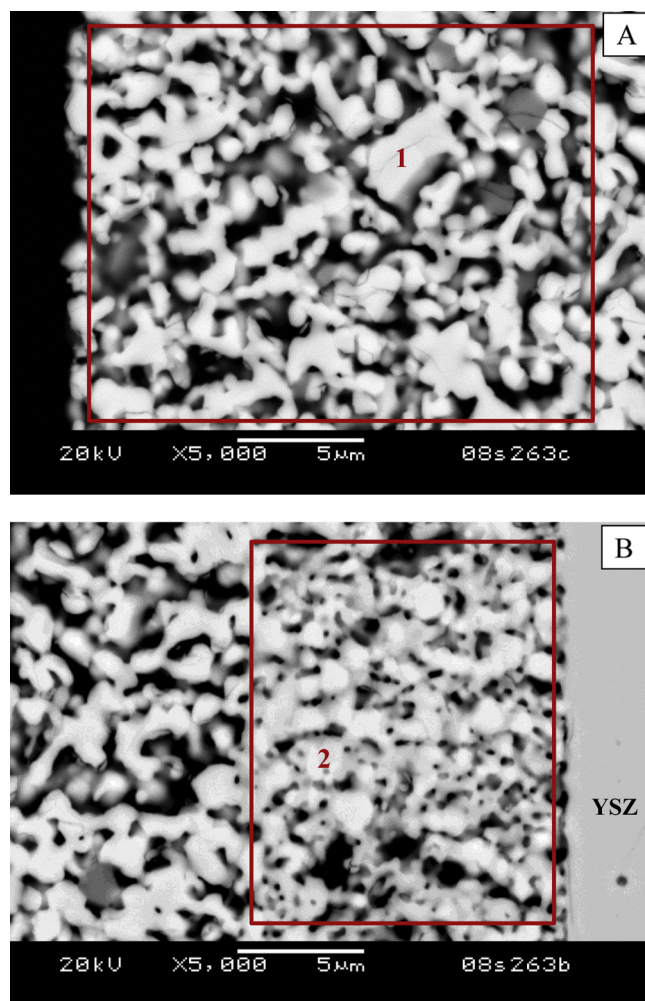
Fig. 9. Cathode microstructure of the cell before 800 °C 6000 h^{-1} test, (A) LSM contact layer (area #1), and (B) active layer of LSM–YSZ composite near YSZ electrolyte (area #2). Chemical compositions of selected areas (#1 and #2) are listed in Table 6.

(Fig. 9B). EDS analyses of the active layer clearly confirmed the presence of Cr in the middle cell, which showed large degradation as compared to the top cell where no Cr was detected. The source of Cr was likely from the uncoated anode interconnect plate as well as poorly coated edges when the glass seal failed. Cr was only detected

Fig. 10. Cathode microstructure of the middle cell (with poor electrochemical performance, see Ref. [30]) of the 3-cell short stack after 800 °C 6000 h^{-1} test, (A) LSM contact layer (between areas #1 and #2), and (B) active layer of LSM–YSZ composite near YSZ electrolyte (between areas #3 and #6). Chemical compositions of selected areas (#1–#6) are listed in Table 7.

Table 6
Chemical analyses of cathode areas #1 and #2 in Fig. 9 before the long-term test.
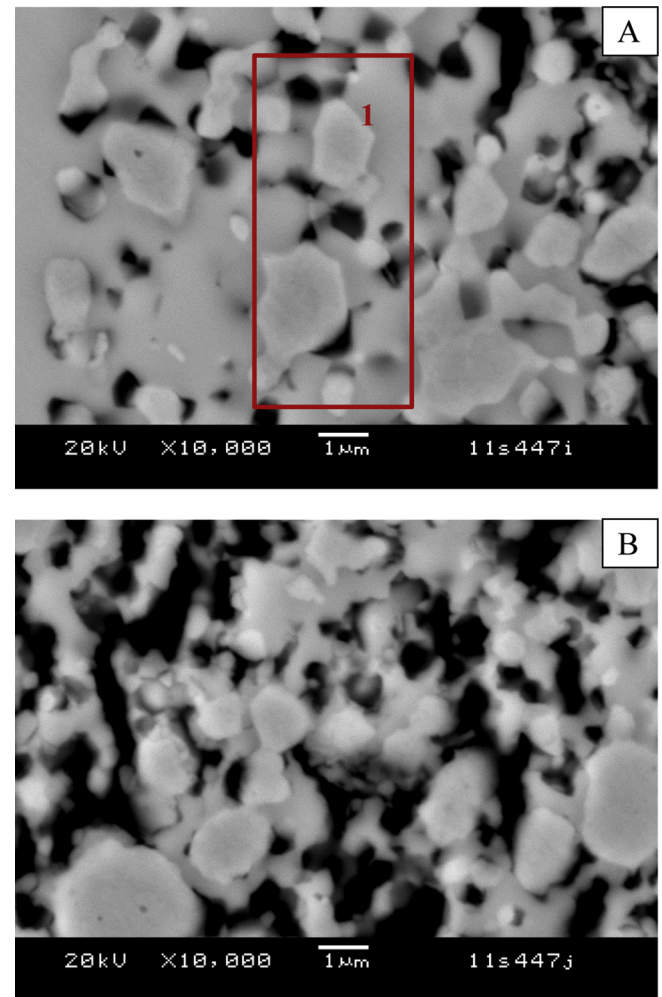
Spot#	O	Cr	La	Sr	Mn	Y	Zr
1	32.22		25.78	7.50	34.50		
2	42.25		11.19	2.58	15.01	3.88	25.09

LSM/YSZ composite, the microstructure exhibited some changes after the long-term test, especially the middle cell (Fig. 10B), where some fine pores seemed filled with gray phases as compared to the cell before testing, where the fine pores were black in color

Table 7
Chemical analyses of cathode areas #1–#6 in Fig. 10 after 800 °C 6000 h^{-1} (the sample was from middle cell of the stack which showed poor performance with rapid degradation (Ref. [30])).

Spot#	O	Cr	La	Sr	Mn	Y	Zr	Ni
1	64.35		14.30	3.90	17.45			
2	59.98		16.39	4.20	19.43			
3	67.95	0.45	5.48	1.10	6.75	3.17	15.10	
4	68.06	2.08	5.54	1.15	7.83	2.93	12.40	
5	68.47	3.97	4.87	0.98	7.19	2.32	11.93	0.26
6	68.03	7.80	4.22	0.68	5.78	2.16	10.99	0.35

Fig. 11. Microstructure of anode after 800 °C 6000 h^{-1} cell test, (A) active anode near YSZ electrolyte, (B) anode support close to active anode, and (C) anode support near the outer surface (~500 μm away from (B)). EDS of the area scan #1 (A) and #2 (C) is listed in Table 8.

in the active LSM/YSZ cathode layer. No Cr was detected in the outer LSM cathode (~ 15 µm on the cell) as well as the thick (~ 500 µm) LSM contact paste added on cell during stack assembly, and the Cr concentration increased near the YSZ electrolyte. For example, Cr was 7.8 at% at the interface, 4.0 at% (~ 5 µm from YSZ), 2.1 at% (~ 10 µm), and ~ 0.5 at% (~ 15 µm) as listed in Table 7. Similar results were also reported for button cell performance of LSM cathode with Cr-containing alloys such as Crofer22APU [8] and ZMG232 [15]. Cr was only detected at the cathode/electrolyte interface not within the bulk LSM cathode or contact paste [8,15]. They attributed the lack of reaction between LSM and the volatile species of $CrO_2(OH)_2$ to the unfavorable thermodynamics for a displacement reaction to form $La_{0.8}Sr_{0.2}Mn_{1-x}Cr_xO_3$ [8] or a kinetically slow process [18], and the favorable reduction reaction at electrolyte/cathode interface or the triple phase boundary to form Cr_2O_3 as below [15]

$$2CrO_2(OH)_2(g) + 6e^- \rightarrow Cr_2O_3(s) + 2H_2O(g) + 3O^{2-}$$

$$2CrO_3(g) \rightarrow Cr_2O_3(s) + 1.5O_2(g)$$
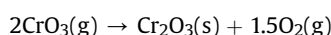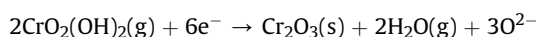
The volatile Cr-containing species could also react with Sr-containing cathode to form $SrCrO_4$; however, the chromate formation was favorable for cathodes containing less stable tetravalent ions such as Fe^{4+} or Co^{4+} as in LSCF [18].

Microstructures at the anode side were also characterized; three areas were examined: active anode layer (next to YSZ electrolyte), anode support near active anode layer, and anode support near the outer surface, as shown in Fig. 11A, B, and C, respectively. chemical analyses for selected areas are listed in Table 8. No Cr was detected within these areas, consistent with thermodynamic calculations that Cr_2O_3 was the most favorable phase at the fuel side without forming volatile species in the reducing and humid environment, and also the oxidizing (instead of reducing) potential at the triple phase boundaries. No discernable coarsening of Ni particles was found which could lead to reduced triple phase boundaries and loss of connectivity between Ni grains, which could contribute to cell degradation. This also appeared consistent with the impedance measurement of the top cell in that the ohmic part was fairly constant during the 6000 h test, as shown in Fig. 12, with the cell's major increase in impedance coming from the polarization part. The ohmic resistance only increased a few milli-ohms in the first ~ 500 h and then remained almost unchanged after that. As mentioned in a previous section, the conductivity of Cr_2O_3 is about $\sim 10^{-3}$–10^{-4} S cm^{-1} at 800 °C, and the thickness of the Cr oxide scale was about 5 µm at the end of test (Fig. 4B). For an interconnect plate of 25 cm^2 and initial oxide scale of a few micron thick, one can estimate the increase in ohmic resistance to be 10–100 mΩ, much greater than the observed value of ~ 2 mΩ. This suggested that the majority of interfacial microstructure of spot-welded Ni wires on AISI441 interconnect plates would be like Fig. 6A where the central portion of the weld was free of a thick and continuous Cr_2O_3 oxide scale, instead of Fig. 6B. The small increase in ohmic part was not clear but likely from the cathode side on the (Mn,Co)-spinel coated interconnect plate.

In addition to Cr-poisoning, several other mechanisms have been investigated as potential cathode degradation mechanisms: microstructure coarsening, phase decomposition, layer spallation,
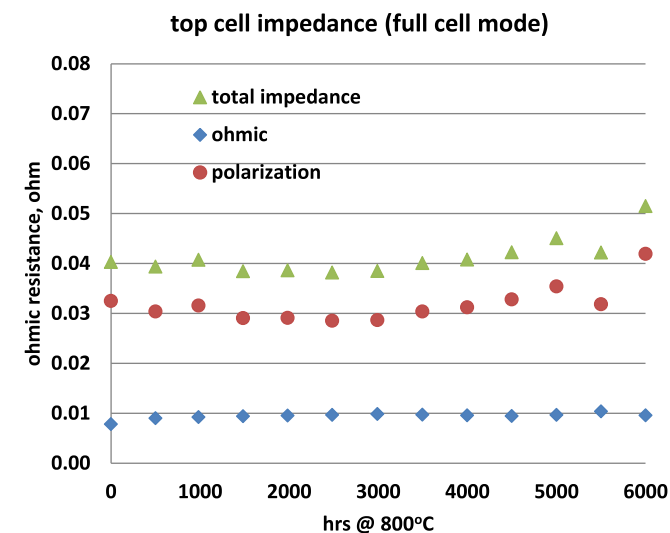
and reaction with electrolyte to form insulating phases [37]. As discussed before, close examination of the microstructure and electrolyte interface showed no discernable coarsening or spallation. Chemical reactions between LSM and YSZ have been studied and a comprehensive review was given by Yokokawa [38]. Insulating phases of $SrZrO_3$ and $La_2Zr_2O_7$ have been identified as possible causes for degradation [38,39], and found likely to form during the initial cathode sintering at high temperatures. On the other hand, $La_2Zr_2O_7$ has been found to form at low (750 °C) operation temperature under high overpotentials (>300 mV) conditions even if it did not form during initial sintering processes [40]. Close examination at the cathode/electrolyte interface of the top and middle cells (Figs. 8B and 10B) revealed no discernable precipitates of $SrZrO_3$ and $La_2Zr_2O_7$. The area scans near the electrolyte interface all showed ratios of Sr/Zr and La/Zr much less than the theoretical ratio of 1 for $SrZrO_3$ and $La_2Zr_2O_7$ (Tables 5 and 7) suggesting that neither of these phases formed during the 6000 h operation.

4. Summary and conclusion

A generic solid oxide fuel cell stack test fixture was developed to evaluate candidate materials and processing under realistic conditions. In this Part III, detailed microstructure analysis was conducted on a Ce-(Mn,Co)-spinel conductive coating, alumina coating, ferritic stainless steel AISI441, Ni current collector, electrodes, and potential Cr poisoning issues. After an 800 °C 6000 h^{-1} test, Ce-modified (Mn,Co)-spinel coating showed improved densification with some diffusion of Cr into the spinel coating. No spallation of the spinel coating or the underneath Cr-oxide scale was found. The strong adhesion was attributed to the tortuous mechanical interlocking. At the metal interface, some segregation of Si and Ti was observed; however, no continuous layer formed. Regarding the protective alumina coating on perimeter sealing areas of AISI441 interconnect or window frame plates, the coating's microstructure appeared more dense and thick at the air side as compared to the fuel side. The alumina coating also remained strongly bonded to the metal substrate. A small amount of Cr was found in the alumina coating. Cr concentration analysis within the metal was also conducted to address the potential Cr-depletion issue for long-term durability. Results showed a small decrease of

Fig. 12. Impedance of the top cell during the long-term (6000 h) stability test at 800 °C. Note the total impedance included the cell, contact materials, and two interconnect plates, i.e., between the top cathode IC plate and the 1st full IC plate (Fig. 1).

Table 8
Chemical analyses of anode after 800 °C 6000 h^{-1} test (referring to Fig. 11A and C).

Area#	O	Ni	Y	Zr	Cr
1	51.10	22.53	4.67	21.70	
2	52.03	25.71	1.66	21.12	

Cr content near the coating interface, implying the effectiveness of the alumina coating. Characterization of current collector Ni wires showed circumferential pores, likely due to redox reactions. At the spot-welded interfaces with the AISI441 substrate, a thin non-continuous as well as thick and continuous Cr-oxide scale was observed. Analysis of the change of ohmic resistance from impedance spectra suggested that the majority of Ni welded points did not form the thick, continuous, and less conductive scale. The microstructure of the cathode and anode was also examined. No Cr was detected in the LSM contact materials for both the top and middle cells. However, Cr was detected within the active cathode layer and the concentration increased near the YSZ electrolyte interface for the middle cell, which showed large degradation. No or very little (close to detection limit) Cr was found in the top cell which showed the lowest overall degradation of the three cells. EDS analysis near YSZ electrolyte interface indicated no formation of the insulating phases of $SrZrO_3$ or $La_2Zr_2O_7$. Overall, the Ce-(Mn,Co) spinel coating, alumina coating, and AISI441 steel showed the desired long-term stability and the developed generic stack fixture proved to be a useful tool to validate candidate materials for SOFC applications.

Acknowledgment

References

[1] N.Q. Minh, J. Am. Ceram. Soc. 76 (3) (1993) 563–588.
[2] B.C.H. Steele, J. Mater. Sci. 36 (2001) 1053–1068.
[3] A. Khandkar, S. Elangovan, J. Hartvigsen, D. Rowley, R. Privette, M. Tharp, in: S.C. Singhal, M. Dokiya (Eds.), Solid Oxide Fuel Cells (SOFC VI) Proceedings of the Sixth International Symposium, The Electrochemical Society, Proceedings, vol. 99-19, 1999, pp. 88–94.
[4] Z. Yang, G.-G. Xia, C.-M. Wang, Z. Nie, J. Templeton, J.W. Stevenson, P. Singh, J. Power Sources 183 (4) (2008) 660–667.
[5] J. Rufner, P. Gannon, P. White, M. Deibert, S. Teintze, R. Smith, H. Chen, Int. J. Hydrogen Energy 33 (7) (2008) 1392–1398.
[6] P.D. Jablonski, C.J. Cowen, J.S. Sears, J. Power Sources 195 (5) (2010) 813–820.
[7] S. Fontana, R. Amendola, S. Chevalier, P. Piccardo, G. Caboche, M. Viviani, R. Moslins, M. Sennour, J. Power Sources 171 (4) (2007) 652–662.
[8] S.P. Simner, M.D. Anderson, G.-G. Xia, Z. Yang, L.P. Pederson, J.W. Stevenson, J. Electrochem. Soc. 152 (4) (2005) A740–A745.
[9] N. Oishi, T. Namikawa, Y. Yamazaki, Surf. Coat. Technol. 132 (1) (2008) 58–64.
[10] S. Fontana, S. Chevalier, G. Caboche, J. Power Sources 191 (1) (2009) 136–145.
[11] Z. Yang, K.S. Weil, D.M. Paxton, J.W. Stevenson, J. Electrochem. Soc. 159 (9) (2003) A1188–A1201.
[12] W.N. Liu, X. Sun, E. Stephens, M.A. Khaleel, J. Power Sources 189 (7) (2009) 1044–1050.
[13] F. Wiener, M. Bram, H.P. Buckkremer, D. Sebold, J. Mater. Sci. 42 (6) (2007) 2643–2651.
[14] A. Holt, P. Kofstad, Solid State Ionics 69 (1) (1994) 127–136.
[15] K. Fujita, K. Ogasawara, Y. Matsuzaki, T. Sakurai, J. Power Sources 131 (1) (2004) 261–269.
[16] S. Taniguchi, M. Kadowaki, H. Kawamura, T. Yasuo, Y. Akiyama, Y. Miyake, T. Saitoh, J. Power Sources 55 (1) (1995) 73–79.
[17] T. Komatsu, R. Chiba, H. Arai, K. Sato, J. Power Sources 176 (1) (2008) 132–137.
[18] H. Yokokawa, T. Horita, N. Sakai, K. Yamaji, M.E. Brito, Y.-P. Xiong, H. Kishimoto, Solid State Ionics 177 (7) (2006) 3193–3198.
[19] Y.D. Zhen, A.I. Tok, S.P. Jiang, F.Y.C. Boey, J. Power Sources 170 (1) (2007) 61–66.
[20] J. Wu, Y. Jiang, C. Johnson, X. Liu, J. Power Sources 177 (2) (2008) 376–385.
[21] W. Wei, W. Chen, D.G. Ivey, J. Power Sources 186 (2) (2009) 428–434.
[22] J.P. Choi, K.S. Weil, Y.M. Chou, J.W. Stevenson, Z.G. Yang, Int. J. Hydrogen Energy 36 (7) (2011) 4549–4556.
[23] Z. Yang, G.-G. Xia, X.-H. Li, J.W. Stevenson, Int. J. Hydrogen Energy 32 (5) (2007) 3648–3654.
[24] Z. Yang, G.-G. Xia, S.P. Simner, J.W. Stevenson, J. Electrochem. Soc. 152 (9) (2005) A1896–A1901.
[25] Z. Yang, G. Xia, Z. Nie, J. Templeton, J.W. Stevenson, Electrochem. Solid-state Lett. 11 (8) (2008) B140–B143.
[26] J.W. Stevenson, Z.G. Yang, G.G. Xia, Z. Nie, J.D. Templeton, J. Power Sources 231 (1) (2013) 256–263.
[27] Y.-S. Chou, J.W. Stevenson, P. Singh, J. Electrochem. Soc. 154 (7) (2007) B644–B651.
[28] Z. Yang, K.D. Meinhardt, J.W. Stevenson, J. Electrochem. Soc. 150 (8) (2003) A1095–A1101.
[29] Y.-S. Chou, J.W. Stevenson, P. Singh, J. Power Sources 185 (2) (2008) 1001–1008.
[30] Y.-S. Chou, J.W. Stevenson, J.-P. Choi, J. Power Sources (2013). Submitted for publication.
[31] Y.-S. Chou, J.W. Stevenson, J.-P. Choi, J. Power Sources 250 (2014) 166–173.
[32] Y.-S. Chou, J.W. Stevenson, J.-P. Choi, Int. J. Appl. Ceramic Technol. 8 (1) (2011) 23–32.
[33] P.Y. Hou, J. Stringer, J. Electrochem. Soc. 134 (7) (1987) 1836–1849.
[34] D.E. Alman, C.D. Johnson, W.K. Collins, P.D. Jablonski, J. Power Sources 168 (2) (2007) 351–355.
[35] J.-H. park, K. Natesan, Oxid. Met. 33 (1–2) (1990) 31–54.
[36] G. Orsello, G. Disegna, K. Litzinger, R. Basel, M. Cali, M. Sentrelli, in: Proceedings of the 7th European SOFC Forum European Fuel Cell Forum, Oberrohrdoft, Switzerland, 2006. File No. A071.
[37] H. Yokokawa, H. Tu, B. Iwanschitz, A. Mai, J. Power Sources 182 (2) (2008) 400–412.
[38] H. Yokokawa, Ann. Rev. Mater. Res. 33 (2003) 581–610.
[39] A. Mitterdorfer, L.J. Gauckler, Solid State Ionics 111 (1) (1998) 185–218.
[40] A. Hagen, R. Barfod, P.V. Hendriksen, Y.-L. Liu, S. Ramousse, J. Electrochem. Soc. 153 (6) (2006) A1165–A1171.